Tunable helical crystals

R. A. Niyazov [1,2] D. N. Aristov [1,2,3] and V. Yu. Kachorovskii [2]
[1]*NRC "Kurchatov Institute", Petersburg Nuclear Physics Institute, Gatchina 188300, Russia*
[2]*Ioffe Institute, 194021 St. Petersburg, Russia*
[3]*Department of Physics, St. Petersburg State University, St. Petersburg 199034, Russia*

(Received 5 June 2023; accepted 11 August 2023; published 22 August 2023)

We consider a superlattice formed by tunnel-connected identical holes, periodically placed in a two-dimensional topological insulator. We study tunneling transport through helical edges of these holes and demonstrate that the band structure of such helical crystal can be controlled by both gate electrodes and external magnetic filed. For integer and half-integer values of dimensionless magnetic flux through the holes, the spectrum possesses Dirac points whose positions and velocities can be tuned by gates. The deviation of magnetic flux from these special values by $\delta\phi$ makes the Dirac cones massive, with the gap value $\Delta \propto |\delta\phi|$. At certain gate-dependent values of $\delta\phi$ different Dirac points converge to a double Dirac point and then disappear with further increase of $\delta\phi$. Interaction between carriers may lead to strong renormalization of parameters α and β controlling total tunnel coupling between holes and spin flip tunneling processes, respectively. We plot the renormalization flow in the plane (α, β) and demonstrate *multicritical* behavior of the crystal—there is a multicritical fully unstable fixed point separating three different phases: independent rings, independent shoulders, and perfect spin-flip channels. We also find that defects in the crystal may lead to a formation of topologically protected qubits, which are not destroyed by temperature and can be also manipulated both by gates and by magnetic field. The possibility of purely electrical high-temperature control of the qubits opens a wide avenue for applications in the area of quantum computing.

DOI: 10.1103/PhysRevB.108.075424

I. INTRODUCTION

One of the hot topics actively discussed in the last decade is the electrical and optical properties of topological insulators, i.e., materials that are insulating in the bulk and have conducting states at the boundary [1–3]. In particular, in two-dimensional (2D) topological insulators, nontrivial bulk band topology results in appearance of helical one-dimensional (1D) states that carry a current along the sample edges without dissipation. The electron propagation in such 1D channels is characterized by a certain helicity, i.e., electrons with opposite spin propagate in opposite directions. As a remarkable consequence, scattering by nonmagnetic impurities is forbidden, and precisely because of this property, there is no dissipation in such channels.

The most well-known implementation of 2D topological insulators is quantum wells in HgTe-based compounds, where topological properties were predicted theoretically [4,5] and confirmed by a series of experiments including measurements of conductance of the edge states [6] and experimental evidence of the nonlocal transport [7–10].

One of the new and promising areas of research is the interferometry based on helical 1D channels. The most interesting possibilities arise in the presence of a magnetic field, which controls interference, due to the Aharonov-Bohm (AB) effect. This effect manifests itself in the bulk properties of 2D topological insulators [11–15] as well as in the helical edge state (HES) systems and interferometers based on them [15–21].

The interference is usually suppressed at high temperature T. However, in the HES-based systems this limitation is sufficiently soft, particularly due to progress in fabrication of high-quality 2D topological insulators. Specifically, for good quantization, T should be much smaller than the bulk gap of the topological insulator. The quantum spin Hall effect was first observed in structures based on HgTe/CdTe [6] and InAs/GaSb [24], where the bulk gap is rather small, less than 100 K. Substantially large values of the gap of order of 500 K were observed in WTe_2 [25]; while a bulk gap of about 0.8 eV was demonstrated in bismuthene grown on a SiC (0001) substrate [26,27] (see also recent discussion in Ref. [28]). These experiments indicate the possibility of topologically protected transport through helical channels even at room temperature. One could also naively expect that interference is damped when T is larger than the level spacing. As was recently demonstrated theoretically [18–21], this is not the case for AB HES-based interferometers, where interference survives even for the case $T \gg 2\pi v_F/(L_1 + L_2)$ where $L_{1,2}$ are lengths of the interferometer shoulders and v_F is the Fermi velocity. This implies that the interference effects in the HES-based systems can be studied at relatively high temperatures practically relevant for various applications.

One of the promising direction of further research is the study of the HES-based metamaterials such as helical crystals. First experimental realizations of such systems were reported recently[22,23]. In these works, the transport properties of an array of holes chemically etched in the layer of topological material (see Fig. 1) were studied. Two different types of AB

 ©2023 American Physical Society

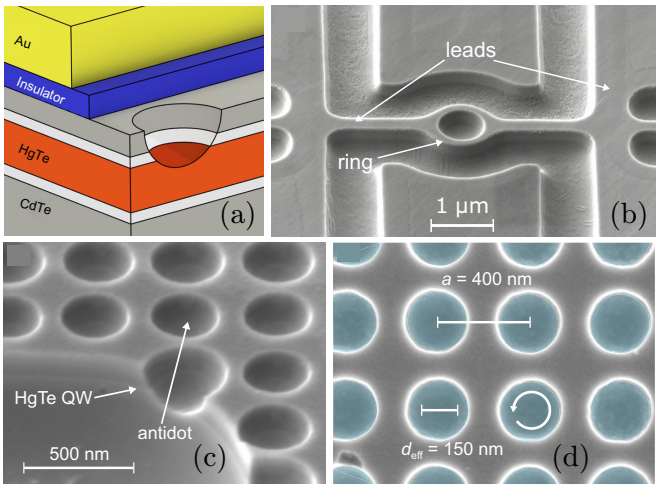

FIG. 1. Various structures based on antidots (etched holes) in the topological insulator. (a) Etched hole in HgTe/CdTe quantum well. (b) Single etched hole and etched channel connected to leads. (c) Antidot lattice in 8-nm width HgTe quantum well. (d) Helical crystal formed by HES on the boundaries of holes. Panel (a) is adopted from [22]; [(b)–(d)] are adopted from [23].

magnetosocillations with the periods h/ec and $h/2ec$ were observed.

The distance between holes in these experiments was sufficiently large, so the holes were not tunnel connected. On the other hand, similar structures with a shorter distance and, therefore, stronger tunnel coupling between neighboring etched holes could demonstrate tunneling transport. Moreover, tunneling barriers between holes can be controlled by gate electrodes. This way, by using 2D topological insulator with etched holes one can fabricate one- or two-dimensional array of tunnel-coupled HES, i.e., a helical crystal tunable by gate electrodes.

In this paper, we consider the simplest realization of the helical crystal, namely, 1D periodic array of closely placed identical etched holes. Specifically, we consider transport through the superlattice formed by HES existing on the boundaries of these etched holes and coupled to each other by contacts, characterized by general scattering matrix, see Fig. 2. The most important property of such a crystal is its tunability. The band structure of the crystal can be controlled by both gate electrodes and external magnetic field. Indeed, the external magnetic field can change flux through a hole thus changing the interference conditions. An additional control is achieved by using different types of gate electrodes (see Fig. 3). Modern technology allows one to apply both back gate covering all system or part of the

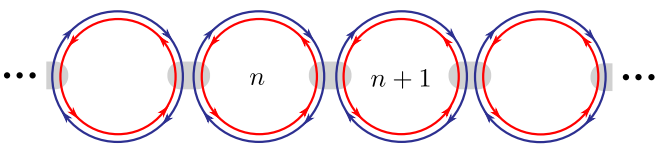

FIG. 2. Chain of helical rings with HES (shown by red and blue color) coupled by tunneling or ballistic contacts (shown by grey color).

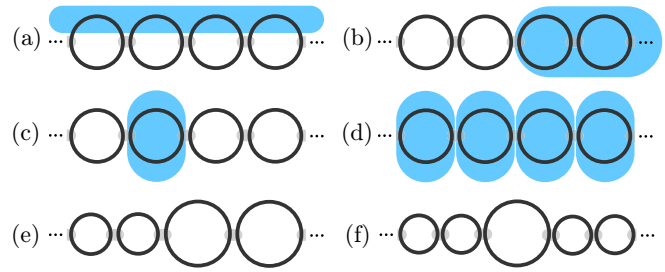

FIG. 3. [(a)–(d)] Various gate configurations (gates are shown by blue color) allowing to tune the crystal. (a) Control of up-down symmetry. (b) Control of right-left symmetry. (c) Voltage shift of an individual ring. (d) Back gate controlling Fermi level and tunneling transparency of the contacts between rings. [(e),(f)] Defects in the crystal: (e) a wall separating rings of different radii encompassing different fluxes, (f) "defect" ring of large radius with a higher flux.

system and individual gates to holes thus creating "defects" in the crystal structure or periodic modulation of the structure. Importantly, tunnel coupling is not the only way to connect HES belonging to different etched holes into a crystal. Effective coupling between holes in the regime of bulk insulator can be also realized by fabricating ballistic contacts between holes made from normal (nontopological) materials. Then, by using special configuration of the gate electrodes one could change transparency (scattering matrix) of such contacts.

We will demonstrate that the variation of magnetic field allows one to create Dirac points (DPs) in the spectrum. Such points appear at special values of the field corresponding to integer or half-integer magnetic flux quantum through the hole. The positions and velocities of the Dirac cones are tuned by gates while deviation of the flux from the special values leads to formation of gaps, i.e., generation of the finite mass of the Dirac fermions (see Fig. 4). With further deviation of the dimensionless flux from the integer or half-integer values, different DPs and corresponding massive Dirac cones can converge forming a double DP. In the vicinity of such point there are two massive Dirac cones that disappear,

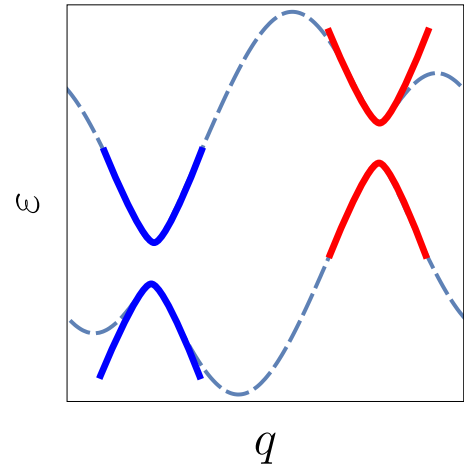

FIG. 4. Schematical dispersion of a band of the helical crystal. Two massive Dirac cones are marked by blue and red color.

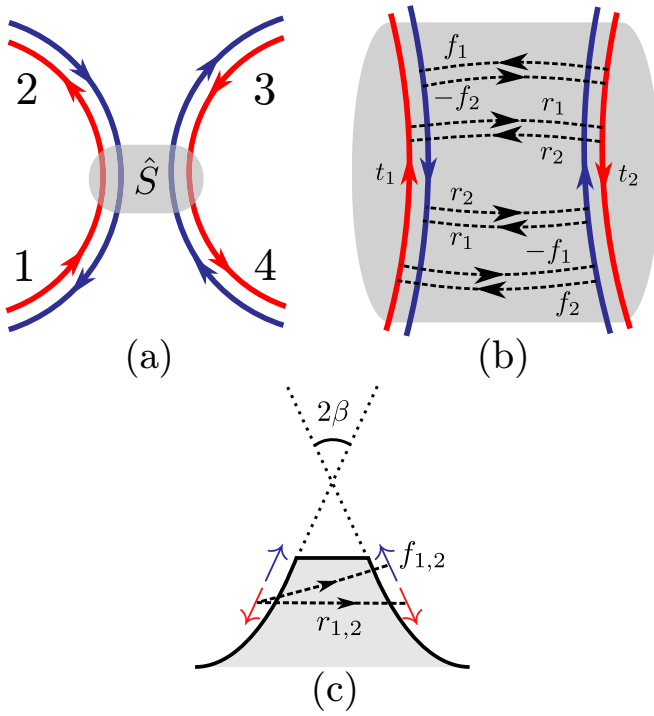

FIG. 5. (a) Junction between two neighboring rings. (b) Amplitudes, t_i, r_i, f_i $(i = 1, 2)$, of different scattering processes are described by elements of $\hat{S}$ matrix [Eq. (2)]. (c) For nonzero angle β, the spin-flip processes are allowed with the amplitudes $f_i \propto \sin\beta$.

when flux deviation becomes higher than some value. We also find that defects in the crystal [see Figs. 3(e) and 3(f)] may lead to emergence of topologically protected states of the Volkov-Pankratov type [29]. At some conditions specified below, these Volkov-Pankratov states are double degenerate. However, the degeneracy can be lifted by changing magnetic field or, more importantly, in a purely electrical way, by changing potentials of gates. This means formation of a topologically protected qubit, which can be manipulated by gates.

II. MODEL

Let us specify our model. We study an 1D array of antidots (etched holes) on the surface of the 2D spin Hall insulator. HES exist at the boundaries of the holes. Electrons propagate along boundaries of the holes thus forming a chain of identical helical rings of length L connected in series (see Fig. 2). Each ring contains clockwise- and counterclockwise moving electrons with energy E, and momentum $k = E/v_F$, having spins opposite at each point. We assume the presence of the external magnetic field and piercing each ring by flux Φ.

We assume that X junction between two neighboring rings with four scattering channels (see Fig. 5) is described by the scattering matrix $\hat{S}$ preserving symmetry with respect to time inversion [30,31],

$$C'_\alpha = S_{\alpha\beta} C_\beta, \quad \alpha, \beta = 1, 2, 3, 4; \tag{1}$$

$$\hat{S} = \begin{pmatrix} 0 & t_1 & f_1 & r_1 \\ t_1 & 0 & r_2 & f_2 \\ -f_1 & r_2 & 0 & t_2 \\ r_1 & -f_2 & t_2 & 0 \end{pmatrix},$$

$$t_j = t e^{i\tau_j}, \quad f_j = f e^{i\phi_j}, \quad r_j = i r e^{i\gamma_j}. \tag{2}$$

Here C'_α and C_β are amplitudes of out-going and incoming waves, respectively, and t, f, r are real valued. The elements of the scattering matrix obey

$$t^2 + r^2 + f^2 = 1, \quad \tau_1 + \tau_2 = \phi_1 + \phi_2 = \gamma_1 + \gamma_2, \tag{3}$$

due to unitarity. One can show that the spectrum of the crystal depends only on combinations $\tau_1 + \tau_2$ and $\phi_1 + \phi_2$, so that without loss of generality and using (3) one can choose

$$\tau_1 = \tau_2 = \phi_1 = \phi_2 = \frac{\gamma_1 + \gamma_2}{2}. \tag{4}$$

Next, we introduce the transfer matrix $\hat{T}$ describing a transition from nth to $(n+1)$th cell of the helical crystal (see Appendix A),

$$\hat{T} = \hat{P}_0 \hat{T}_0 \tag{5}$$

where T_0 and P_0 describe transitions through the contact and the ring, respectively.

The matrix of contact T_0 corresponds to the matrix $\hat{S}$ and expresses the wave function amplitudes in the $(n+1)$th ring (right after the contact) via the amplitudes in nth ring (right before the contact). It can be written as

$$\hat{T}_0 = \hat{D}\hat{T}_r\hat{D},$$

$$\hat{T}_r = \frac{1}{1-t^2}\begin{pmatrix} ir & ft & -f & -irt \\ -ft & -ir & irt & f \\ -f & -irt & ir & ft \\ irt & f & -ft & -ir \end{pmatrix},$$

$$\hat{D} = \mathrm{diag}[e^{i\gamma_2/2}, e^{-i\gamma_2/2}, e^{i\gamma_1/2}, e^{-i\gamma_1/2}]. \tag{6}$$

The matrix

$$\hat{P}_0 = \mathrm{diag}[e^{i\varphi_b}, e^{-i\varphi_a}, e^{i\varphi_a}, e^{-i\varphi_b}], \tag{7}$$

contains phases acquired inside a ring by moving from the left contact to the right one,

$$\varphi_a = \frac{\varepsilon}{2} - \pi\phi, \quad \varphi_b = \frac{\varepsilon}{2} + \pi\phi, \tag{8}$$

where we introduced dimensionless energy and dimensionless flux,

$$\varepsilon = \frac{EL}{v_F} = kL, \quad \phi = \frac{\Phi}{\Phi_0}, \tag{9}$$

where Φ_0 is the flux quantum.

In Eq. (8) we assumed that etched holes are ring shaped, contacts are placed symmetrically, and energies of the electrons in the up and down parts of the ring are the same. However, by using specific gate configurations [see Fig. 3(a)] one can change energies, which would lead to appearance of two different dimensionless energies, $\varepsilon^{\mathrm{up}} = k^{\mathrm{up}}L$ and $\varepsilon^{\mathrm{down}} = k^{\mathrm{down}}L$ (see Appendix A).

The amplitudes t, r, and f can be parametrized as follows:

$$t = \cos\alpha,$$
$$r = \sin\alpha\cos\beta,$$
$$f = \sin\alpha\sin\beta. \tag{10}$$

Processes corresponding to scattering amplitudes are illustrated in Fig. 5. Amplitudes r and f describe hopping between rings into the states with the same and opposite spin projections, respectively. Physically, α is related to the total probability of such hopping: $r^2 + f^2 = \sin^2\alpha$. The angle 2β is the angle between the spin quantization axes in different helical states [32], and elements r and f are proportional to overlapping of spinors in the neighboring helical edges. For tunneling contact ($\alpha \ll 1$), α is mainly controlled by tunneling distance. The case of ballistic (or metallic) contact, when rings are strongly coupled, corresponds to $\alpha \approx \pi/2$. Parameter β controls spin-flip processes. Indeed, for $\beta = 0$, we get $f = 0$.

III. DISPERSION OF 1D HELICAL CRYSTAL

Next, we derive and analyze the dispersion relation of 1D helical crystal shown in Fig. 2, i.e., the dependence $\varepsilon = \varepsilon(q)$ of the dimensionless energy ε on the dimensionless quasimomentum q measured in units of $1/L$.

A. General dispersion equation

We look for those four-component vectors ψ_j referring to jth ring, which upon the action of transfer matrix return to their form up to a phase factor, that is $\psi_{j+1} = \hat{T}\psi_j = e^{iq}\psi_j$. Hence the band structure of the crystal is found from the following equation:

$$\det[\hat{1}e^{iq} - \hat{T}] = 0, \tag{11}$$

where $\hat{1}$ is 4×4 unit matrix. The resulting dispersion relation $\varepsilon(q)$ is quite complicated and can be found in implicit form by using Eqs. (5), (6), and (7),

$$\begin{aligned}&(\cos\beta\sin(\varepsilon/2 + \pi\phi) + \sin\alpha\cos(q - v/2))\\ &\quad\times(\cos\beta\sin(\varepsilon/2 - \pi\phi) + \sin\alpha\cos(q + v/2))\\ &\quad+ \tfrac{1}{2}\sin^2\beta(\cos^2\alpha\cos 2\pi\phi - \sin^2\alpha\cos v - \cos\varepsilon) = 0.\end{aligned} \tag{12}$$

Here,

$$\varepsilon = kL + \gamma_1 + \gamma_2, \quad v = \gamma_2 - \gamma_1. \tag{13}$$

We note a following general property: if q, ε satisfy Eq. (12), then $q \to q + \pi$, $\varepsilon \to \varepsilon + 2\pi$ also satisfy this equation.

As seen from Eqs. (12) and (13), the sum $\gamma_1 + \gamma_2$ affects only the total energy shift, so that without loss of generality we can set $\gamma_1 + \gamma_2 = 0$. In this case we have

$$\gamma_2 = -\gamma_1 = \frac{v}{2}. \tag{14}$$

In order to understand the physical meaning of the phase v, one can consider different energies at the upper and lower shoulders of the ring. Then, $\hat{P}_0$ is given by a more general equation (A3). One can check that Eq. (12) still holds with

$$\varepsilon = (k^{\rm up} + k^{\rm down})L/2 + \gamma_1 + \gamma_2,$$
$$v = (k^{\rm up} - k^{\rm down})L/2 + \gamma_2 - \gamma_1. \tag{15}$$

Both $k^{\rm up}$ and $k^{\rm down}$ depend on the electron energy E and can be also controlled by the gate voltages, so that $k^{\rm up} - k^{\rm down} \propto U^{\rm up} - U^{\rm down}$, where $U^{\rm up,down}$ are the gate voltages applied to the upper and lower shoulders of the interferometer [see Fig. 3(a)]. Hence, Eq. (12) is equally applicable to the system with complicated gate configurations. The expression for v shows that the difference of gate voltages is equivalent to difference of γ_1 and γ_2. It means that the parameter v controls the up-down asymmetry of the system, arising either due to asymmetry of the contact, $\gamma_2 - \gamma_1$, or due to asymmetric gate voltage configuration ($k^{\rm up} - k^{\rm down} \propto U^{\rm up} - U^{\rm down}$). For simplicity, one can assume that $k^{\rm up} = k^{\rm down} = k = E/v_{\rm F}$. Then, Eq. (12) gives dependence of the dimensionless energy ε on q, while the dependence on v is equivalent on the dependence on the gate voltage difference $U^{\rm up} - U^{\rm down}$. Next, we discuss different limiting cases covered by Eq. (12) and corresponding to different physical situations.

B. Independent rings, $\alpha = 0$

In the absence of the tunneling coupling, i.e., for $\alpha = 0$, the rings are isolated. Hence, all bands of the crystal shrink into the following quantum levels for clockwise- and counterclockwise moving electrons, respectively,

$$\varepsilon_n^+ = 2\pi(n + \phi), \quad \varepsilon_n^- = 2\pi(n - \phi), \tag{16}$$

with integer n [here we do not write the shift of the total dimensionless energy $\gamma_1 + \gamma_2 = 0$; see discussion after Eq. (12)]. As seen from Eqs. (16), the most interesting effects are expected for $\phi = 0$ and $\phi = 1/2$, when levels are doubly degenerate.

For small but finite α ($\alpha \ll 1$), the energy levels (16) evolve into narrow bands, with the width proportional to α. In order to study dependence of bands on ϕ, it is convenient to parametrize the energy levels at $\alpha = 0$ in the following way:

$$\varepsilon_{1,n}^{\rm ir} = 2\pi n + \arccos(\cos 2\pi\phi),$$
$$\varepsilon_{2,n}^{\rm ir} = 2\pi n - \arccos(\cos 2\pi\phi), \tag{17}$$

where label "ir" stands for "independent rings". This parametrization is different from Eq. (16). The key advantage of Eq. (17) is the possibility to describe the avoidance of level crossing, which happens at $\alpha \neq 0$ for $\phi \approx 0$ and $\phi \approx 1/2$ as we demonstrate below (see Fig. 6). We notice that Eq. (17), unlike Eq. (16), is periodic in ϕ and has the property $\varepsilon_{1,n}^{\rm ir} > \varepsilon_{2,n}^{\rm ir}$ for any n and ϕ.

C. Independent shoulders

The case $\alpha = \pi/2$, $\beta = 0$ corresponds to the disconnected upper and lower shoulders of the array. As follows from Eq. (12), there are four branches of dispersion in this case, which are given by

$$\varepsilon_{1,n}^{\rm is} = 2q + 2\pi\phi + v + \pi(4n - 1),$$
$$\varepsilon_{3,n}^{\rm is} = -2q - 2\pi\phi + v + \pi(4n - 1),$$

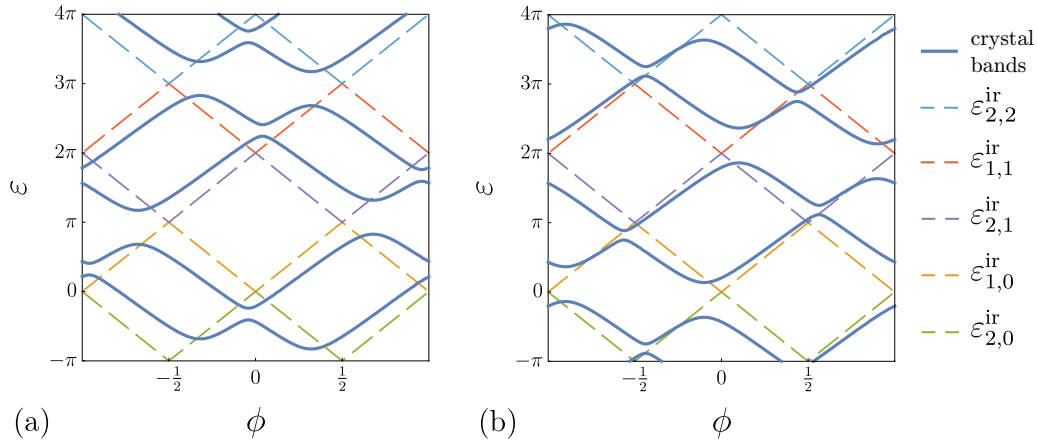

FIG. 6. Dependence of the dimensionless energy in several neighboring bands of helical crystal on the magnetic flux for fixed q at $\alpha = \pi/4$, $v = \pi/3$, and $\beta = 0.6$; (a) $q = \pi/10$, (b) $q = 2\pi/5$. Dashed curves correspond to $\alpha = 0$ and are described by Eq. (17).

$$\varepsilon^{\rm is}_{2,n} = 2q - 2\pi\phi - v + \pi(4n-1),$$
$$\varepsilon^{\rm is}_{4,n} = -2q + 2\pi\phi - v + \pi(4n-1), \qquad (18)$$

where label "is" stands for "independent shoulders". The integer index n corresponds to our consideration of reduced Brillouin zone scheme $q \in (-\pi, \pi)$. For disconnected shoulders, however, the consideration of the extended Brillouin zone scheme $q \in (-\infty, \infty)$ is equally suitable. In the latter case we should set $n = 0$ in right-hand side of Eq. (18) to avoid double counting.

The meaning of four branches is easily understood. They correspond to spin-conserving chiral motion. The branches 1 and 3 correspond to right- and left-moving electrons, respectively, in the upper shoulder. The branches 2 and 4 refer to right- and left-moving electrons, respectively, in the lower shoulder.

D. Spin conserving motion

Let us now generalize the case considered in the previous subsection by assuming that $\alpha \neq \pi/2$ but still $\beta = 0$. This case corresponds to hopping between rings without spin flips. From Eq. (12) we find that there are several solutions found from

$$\sin(\varepsilon/2 + \pi\phi) + \sin\alpha\cos(q - v/2) = 0,$$
$$\sin(\varepsilon/2 - \pi\phi) + \sin\alpha\cos(q + v/2) = 0. \qquad (19)$$

These equations yield four branches of dispersion:

$$\varepsilon^{\rm sc}_{1,n} = -2\arcsin[\sin\alpha\cos(q + v/2)] + 2\pi\phi + \pi(4n),$$
$$\varepsilon^{\rm sc}_{3,n} = 2\arcsin[\sin\alpha\cos(q - v/2)] - 2\pi\phi + \pi(4n-2),$$
$$\varepsilon^{\rm sc}_{2,n} = -2\arcsin[\sin\alpha\cos(q - v/2)] - 2\pi\phi + \pi(4n),$$
$$\varepsilon^{\rm sc}_{4,n} = 2\arcsin[\sin\alpha\cos(q + v/2)] + 2\pi\phi + \pi(4n-2), \qquad (20)$$

where label "sc" stands for "spin conserving". The choice of branches here is done in such a way that $\varepsilon^{\rm sc}_{j,n}$ coincides with $\varepsilon^{\rm is}_{j,n}$ [see Eq. (18)] for $\alpha = \pi/2$ and $(q \pm v/2) \in (0, \pi)$. It is worth noting that for arbitrary q and v, Eqs. (18) and (20) give different parametrization of the spectrum for $\alpha = \pi/2$. Equation (20) is more convenient because it allows to describe the avoidance of level crossing, happening for arbitrary small deviation of α from the value $\pi/2$ [in a full analogy with the difference between Eqs. (16) and (17)].

E. Perfect spin-flip chiral motion

For $\alpha = \pi/2$ and $\beta = \pi/2$, the spectrum does not depend on the flux and is given by

$$\varepsilon^{\rm sf}_{1,n} = 2q + 2\pi n,$$
$$\varepsilon^{\rm sf}_{2,n} = -2q + 2\pi n, \qquad (21)$$

where label "sf" stands for "spin flip." In this case, the chirality is conserved, but the electron jumps between shoulders with flipping the spin direction after transmission of any contact. Such unusual transmission can be induced by the effects of interaction (see Sec. V).

F. Special values of magnetic flux

The spectrum dramatically simplifies for integer and half-integer values of the dimensionless magnetic flux. Most interestingly the Dirac points appear in all bands. These points appear by pairs (one pair per Brillouin zone for any band). They are doubly degenerate for $v = 0$.

Before we turn to the analysis of these special values of the flux, we notice that Eq. (12) is invariant under the replacement

$$\phi \to \phi + 1, \quad q \to q + \pi. \qquad (22)$$

It follows that we can restrict our consideration to the cases $\phi = 0$ and $\phi = 1/2$. Let us find the bands of the crystal exactly at these values of flux.

1. $\phi = 0$

In this case, Eq. (12) is reduced to

$$\sin[\varepsilon/2] = -\sin\alpha\cos(q \pm q_0), \qquad (23)$$

where q_0 $(0 < q_0 < \pi)$ obeys $\cos q_0 = \cos\beta\cos(v/2)$. Solutions of Eq. (23) can be written as

$$\varepsilon^{\phi=0}_{1,n} = 2\pi n + 2\arcsin[\sin\alpha((-1)^{n+1}\cos q\cos q_0$$

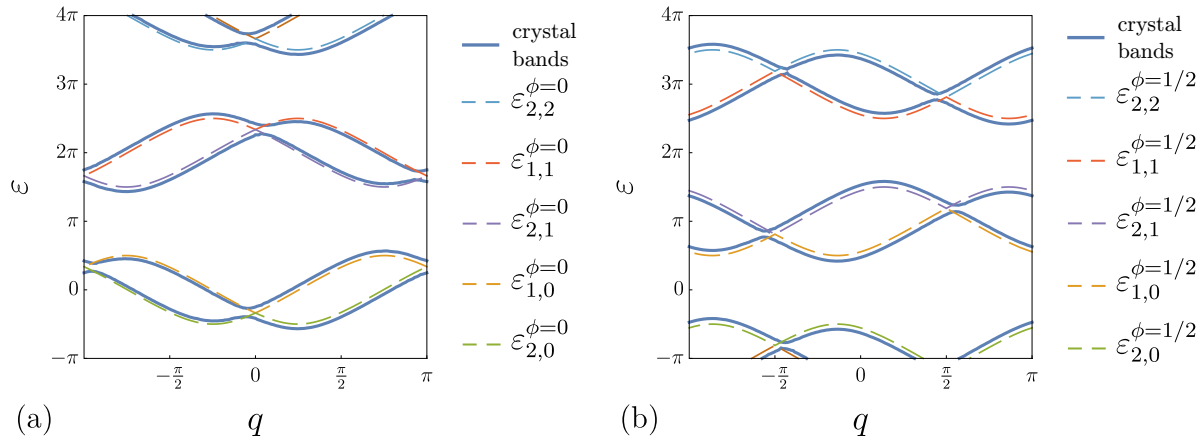

FIG. 7. Several lowest-energy bands of the helical crystal for $\alpha = \pi/4$, $v = \pi/3$, and $\beta = 0.6$. (a) $\phi = 0.05$ [dashed curves corresponds to $\phi = 0$ and are described by Eq. (24)]. (b) $\phi = 0.45$ [dashed curves corresponds to $\phi = 1/2$ and are described by Eq. (27)].

$$+ |\sin q| \sin q_0)],$$
$$\varepsilon^{\phi=0}_{2,n} = 2\pi n + 2\arcsin[\sin\alpha((-1)^{n+1}\cos q\cos q_0 - |\sin q|\sin q_0)], \quad (24)$$

As one can see from these equations, there are DPs in the spectrum corresponding to the condition $\varepsilon^{\phi=0}_{1,n} = \varepsilon^{\phi=0}_{2,n}$. This condition is satisfied for

$$q_{\rm DP} = \pi m \quad (25)$$

with integer m (for the first Brillouin zone we keep $m = 0, 1$ only). Several lowest bands are depicted in the left panel of Fig. 7.

2. $\phi = 1/2$

Substituting $\phi = 1/2$ into Eq. (12) we get

$$\cos[\varepsilon/2] = -\sin\alpha\sin(q \pm q_1), \quad (26)$$

where $\cos q_1 = \cos\beta\sin(v/2)$ and $0 < q_1 < \pi$.

The energy bands found from this equation are given by

$$\varepsilon^{\phi=1/2}_{1,n} = 2\pi n + 2\arccos[-\sin\alpha((-1)^n\sin q\cos q_1 - |\cos q|\sin q_1)],$$
$$\varepsilon^{\phi=1/2}_{2,n+1} = 2\pi n + 2\arccos[-\sin\alpha((-1)^n\sin q\cos q_1 + |\cos q|\sin q_1)]. \quad (27)$$

There are Dirac points in the spectrum corresponding to the condition $\varepsilon^{\phi=1/2}_{1,n} = \varepsilon^{\phi=1/2}_{2,n+1}$. Positions of these points are given by

$$q_{\rm DP} = \frac{\pi}{2} + \pi m, \quad (28)$$

with integer m ($m = 0, -1$ for the first Brillouin zone).

Hence, at special values of the flux, $\phi = 0$ and $\phi = 1/2$, the spectrum demonstrates the existence of Dirac cones. These cones are clearly seen in Fig. 7. Importantly, when the flux deviates from the special values, the DPs move away from the values of q given by Eqs. (25) and (28) and a finite gap appears in the Dirac cones, so that these cones become massive. These points can also converge with changing the flux forming double DPs and then disappear at certain value of the flux.

We discuss the massive Dirac cones and double DPs in more detail in subsequent Secs. III G, III H, and Appendix C.

G. Massive Dirac cones

The dependence on ϕ for $\alpha \neq 0$ and fixed q is shown in the Fig. 6 by thick lines for small value of q (left panel) and for q close to π (right panel). As seen, there is level anticrossing at integer and half-integer values of flux. If we now fix flux values close to these special values, and change q, then we get spectrum of the crystal with the DPs appearing at values of q, which are close to integer values of q/π for integer ϕ and half-integer values of q/π for half-integer values of ϕ as shown in Fig. 7.

Let us first discuss the spectrum for the case of nearly integer value of flux. The position of DPs can be represented as :

$$\varepsilon_{\rm DP} = 2\pi n - 2(-1)^{n+m+p}\arcsin[\sin\alpha\cos\beta\cos(v/2)],$$
$$\phi_{\rm DP} = p, \quad q_{\rm DP} = \pi m, \quad (29)$$

here $m = (-1,\ 0)$, and $n,\ p$ are integer. The spectrum close to all DPs can be written in the following form:

$$\delta\varepsilon = \pm\sqrt{(A\delta q + B\delta\phi)^2 + C^2(\delta\phi)^2} \quad (30)$$

where, $\delta\varepsilon$, δq, and $\delta\phi$ are counted from their values exactly at DPs, Eq. (29).

As follows from this equation, the gap in the spectrum is given by

$$\Delta = 2C|\delta\phi|. \quad (31)$$

The coefficients B and C are the same for all DPs with ϕ close to integer values, while A has different sign and the same

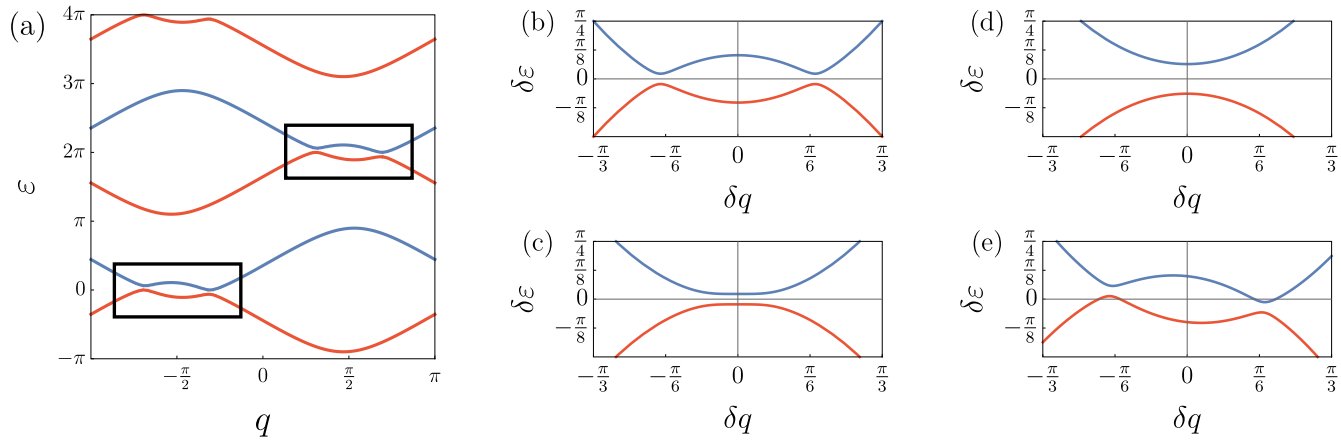

FIG. 8. (a) Two close massive Dirac cones for each band $\phi = 0.2$, $\beta = 0.1$, and $v = 3$ [spectrum is found from Eq. (36)]. Spectrum in vicinity of the convergence point [see Eq. (C5)]. (b) Symmetric double DP for negative $\delta\phi$ ($\delta\phi = -0.05$,) $\beta = 0.05$, and $\delta v = 0$. (c) Exact convergence of two DPs at $\delta\phi = 0$, $\beta = 0.05$, and $\delta v = 0$. (d) Disappearance of pair of DPs and increase of gap at positive $\delta\phi$ ($\delta\phi = 0.03$), $\beta = 0.05$, and $\delta v = 0$. (e) Asymmetric spectrum for negative $\delta\phi$ and nonzero δv: $\delta\phi = -0.06$, $\beta = 0.05$, and $\delta v = -0.2$. Curves in all panels are plotted for $\alpha = \pi/4$.

absolute value for different DPs,

$$A = 2\,(-1)^{n+m+p}\sin\alpha\,\sqrt{\frac{1-[\cos(v/2)\cos\beta]^2}{1-(\cos(v/2)\cos\beta\sin\alpha)^2}},$$
$$B = \frac{2\pi\cos\beta\sin(v/2)}{\sqrt{1-[\cos(v/2)\cos\beta]^2}},$$
$$C = \frac{2\pi\cos\alpha\sin\beta}{\sqrt{[1-[\cos(v/2)\cos\beta]^2][1-[\cos(v/2)\cos\beta\sin\alpha]^2]}}. \tag{32}$$

We notice that $A \to 0$ for $\alpha \to 0$, thus reflecting the existence of flat bands in this limit [see Eqs. (16) and (17)]. For $\beta = 0$ the chiral channels are decoupled. In this case, $C = 0$ and

$$\delta\varepsilon = |A\delta q + B\delta\phi|. \tag{33}$$

Hence, in this special case we have a gapless spectrum for any $\delta\phi$.

The spectrum for the case of nearly half-integer values of flux ϕ is characterized by a different set of DPs, now written as

$$\varepsilon_{\rm DP} = 2\pi\left(n+\tfrac{1}{2}\right)+2(-1)^{n+m+p}\arcsin[\sin\alpha\cos\beta\sin(v/2)],$$
$$\phi_{\rm DP} = m+\tfrac{1}{2}, \quad q_{\rm DP} = \pi p+\tfrac{\pi}{2}. \tag{34}$$

Remarkably, Eqs. (30) and (32) are still valid, with the replacement $v \to v+\pi$.

H. Converging of the Dirac points

As seen from equations presented in Sec. III G, different massive Dirac cones become closer when flux deviates from integer and half-integer values by a value $\delta\phi$. For certain values of flux these points converge forming a double DP and then disappear with further increase of $\delta\phi$. At the convergence point two branches of the spectrum touch each other, i.e., they coincide and have the same derivative (see Fig. 8).

For simplicity, we limit ourselves below with the case $\beta \ll 1$. For $\beta \equiv 0$, the convergence points appear for four values of the flux, ϕ_j ($j = 1, 2, 3, 4$), given by

$$\phi_1 = 1-\phi_2 = \frac{\arcsin(\sin(v/2)\sin\alpha)}{\pi},$$
$$\phi_3 = 1-\phi_4 = \frac{1}{2}-\frac{\arcsin(\cos(v/2)\sin\alpha)}{\pi}. \tag{35}$$

Close to these convergence points and for $\beta \ll 1$ the spectrum is approximated as

$$\delta\varepsilon = D\delta q \pm \sqrt{4\beta^2\sin^2\alpha+(2\pi\delta\phi+E\delta q^2)^2}, \tag{36}$$

where $|\varepsilon - D\delta q| \sim |\delta\phi| \sim \delta q^2 \sim \beta \ll 1$. Here, $\delta\phi = \phi - \phi_j$, $\delta q = q - q_j$, $\delta\varepsilon = \varepsilon - \varepsilon_j$, where ϕ_j are given by Eq. (35). The positions of convergence points in (q, ε) plane and formulas for coefficients D and E are presented in the Appendix C. The discussion of some limiting cases can be also found there. The spectrum in vicinity of the convergence points, formation of double DP and disappearance of pairs of DP are illustrated in Fig. 8.

I. Band engineering

In this section we briefly summarize the discussion of the previous sections in order to describe different ways to control the electron spectrum. In Fig. 9 we illustrate the evolution of the bands with a variation of different parameters. First of all, we notice that the widths of all bands are proportional to α and there is a pair of two symmetric DPs in each band for special values of the flux [as illustrated in Fig. 9(a) for $\phi = 1/2$]. The energy positions of the DPs are the same provided $v = 0$. Small deviation of ϕ from the value $1/2$ opens small gaps in both Dirac cones [see Fig. 9(b)]. The width of appearing gap, i.e., the mass of the Dirac fermions, is proportional to $|\delta\phi|$ and tends to zero when $\beta \to 0$. Changing parameter v [by using asymmetric gate configuration shown

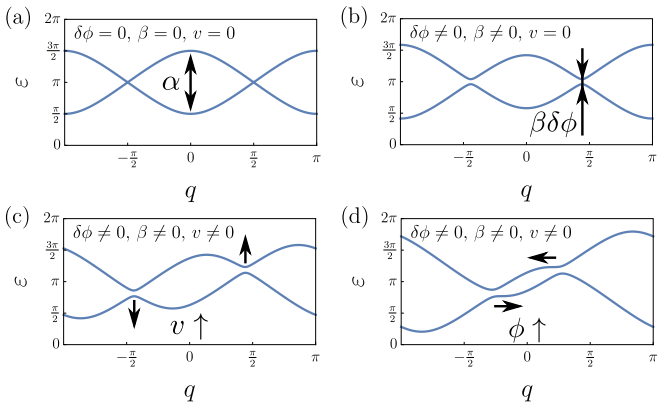

FIG. 9. Schematical picture of the lowest band of the crystal for different values of parameters. (a) Two Dirac cones for $\alpha = \pi/4$, $\delta\phi \equiv \phi - 1/2 = 0$, $\beta = 0$, $v = 0$. (b) Formation of the gap for small deviation of the flux $\delta\phi$ from half-integer value: $\delta\phi = 0.05$, $\beta = 0.6$, $v = 0$. (c) Shifting of energy of the DPs in opposite direction for $v \neq 0$: $\delta\phi = 0.05$, $\beta = 0.6$, $v = \pi/3$. (d) Convergence of the DPs with increasing of $\delta\phi$: $\delta\phi = 0.15$, $\beta = 0.2$, $v = \pi/3$.

in Fig. 3(a)] the energies of the DPs move in opposite directions [see Fig. 9(c)]. With increasing $\delta\phi$ two DPs in a pair converge [see Fig. 9(d)]. Hence one can control spectrum using magnetic field and gate electrodes of different configurations.

IV. TOPOLOGICALLY PROTECTED LOCALIZED STATES

A. Effective Hamiltonian near the Dirac point

Perhaps the easiest way to obtain the effective Hamiltonian near the DPs is to "take square" of the dispersion relation. Namely, instead of (11) we consider the transfer matrix to the next-to-nearest neighbor, which results in the equation

$$\det[\hat{1}e^{i2q} - \hat{T}^2(\varepsilon)] = 0. \tag{37}$$

To be specific, let us consider $\phi \simeq 1/2$, when positions of the DPs read $q_{\rm DP} = \pm\pi/2$, so that $\hat{1}e^{2iq_{\rm DP}} = -\hat{1}$. One can check that $\hat{T}^2 = -\hat{1}$ as well for $q = q_{\rm DP}$ (although $T \neq \hat{1}e^{iq_{\rm DP}}$). This property simplifies expansion near the DPs: $q = \pm\pi/2 + \delta q$, $\varepsilon = \pi + \delta\varepsilon$, $\phi = 1/2 + \delta\phi$, $v = \delta v$ ($\delta\phi \ll 1$, $\delta q \ll 1$, $\delta v \ll 1$). We get

$$\det\left[2i\delta q + \delta\varepsilon\frac{\partial\hat{T}^2}{\partial\varepsilon}\bigg|_{\rm DP} + \delta v\frac{\partial\hat{T}^2}{\partial v}\bigg|_{\rm DP} + \delta\phi\frac{\partial\hat{T}^2}{\partial\phi}\bigg|_{\rm DP}\right] = 0. \tag{38}$$

The Hamiltonian with the same dispersion relation can then be found in the form

$$\mathcal{H}^{(1)}_{\rm eff} = -R^{-1}\left(\frac{\partial\hat{T}^2}{\partial\varepsilon}\right)\bigg|^{-1}_{\rm DP}\left[2i\delta q + \frac{\partial\hat{T}^2}{\partial v}\bigg|_{\rm DP}\delta v + \frac{\partial\hat{T}^2}{\partial\phi}\bigg|_{\rm DP}\delta\phi\right]R. \tag{39}$$

Here, R is chosen so that $\mathcal{H}^{(1)}_{\rm eff}$ is Hermitian. Taking

$$R = \begin{pmatrix} i\tau^\alpha & -i\tau^\alpha\tau^\beta & i & -i\tau^\beta \\ \tau^\beta & 1 & \tau^\alpha\tau^\beta & \tau^\alpha \\ \tau^\alpha\tau^\beta & \tau^\alpha & \tau^\beta & 1 \\ i & -i\tau^\beta & i\tau^\alpha & -i\tau^\alpha\tau^\beta \end{pmatrix},$$
$$\tau^\alpha = \tan(\tfrac{\pi}{4} + \tfrac{\alpha}{2}), \quad \tau^\beta = \tan\tfrac{\beta}{2}, \tag{40}$$

after simple rearrangement we obtain the effective Hamiltonian with the block-diagonal structure

$$\mathcal{H}^{(1)}_{\rm eff} = \begin{pmatrix} \mathcal{H}_1 & 0 \\ 0 & \mathcal{H}_2 \end{pmatrix},$$
$$\mathcal{H}_1 = \delta v\cos\beta\sin\alpha\sigma_0 + 2\pi\delta\phi\cos\alpha\sin\beta\sigma_1 + (2\pi\delta\phi\cos\beta + 2\delta q\sin\alpha)\sigma_3,$$
$$\mathcal{H}_2 = -\delta v\cos\beta\sin\alpha\sigma_0 + 2\pi\delta\phi\cos\alpha\sin\beta\sigma_1 + (2\pi\delta\phi\cos\beta - 2\delta q\sin\alpha)\sigma_3. \tag{41}$$

Here, $\sigma_{1,3}$ are the Pauli matrix and σ_0 is the identity matrix.

Below we will also need corrections to the effective Hamiltonian (41). In order to analyze these corrections, we expand the matrix $\hat{T}^2$ in Eq. (38) up to the next order with respect to small parameters $\delta\phi$, δv, δq, $\delta\epsilon$. The calculations are straightforward but cumbersome and will be presented in detail elsewhere [33]. There are two types of corrections: (i) corrections to $\bar{\mathcal{H}}_1$ and $\bar{\mathcal{H}}_2$, which do not essentially modify the massive Dirac cone spectrum and can be omitted for our purposes and (ii) the block-off-diagonal corrections, which are given by

$$\mathcal{H}^{(2)}_{\rm eff} = \begin{pmatrix} 0 & \hat{V} \\ \hat{V}^\dagger & 0 \end{pmatrix}. \tag{42}$$

With the precision necessary for Sec. IV C below one finds

$$\hat{V} = i(\bar{q}^2 - \pi^2\delta\phi^2\sin^2\beta)\sin 2\alpha\,\hat{\sigma}_3 + \pi^2\delta\phi^2\sin\alpha\sin 2\beta\,\hat{\sigma}_1, \tag{43}$$

where $\hat{\sigma}_i$ ($i = 0, 1, 2, 3$) are the Pauli matrices and $\bar{q}$ is given by Eq. (46).

B. Topologically protected localized states

The block $\mathcal{H}_2$ of the Hamiltonian can be obtained from $\mathcal{H}_1$ by changing $\delta q \to -\delta q$ and $\delta v \to -\delta v$ (or $\alpha \to -\alpha$). The term with δv may be absorbed into an energy shift in each of two blocks,

$$E_1 = -E_2 = -W, \quad W = \delta v\cos\beta\sin\alpha. \tag{44}$$

So we may discuss the block $\mathcal{H}_1$ only. The small wave-vector shift, $\delta q \ll 1$, can be represented as a electron's motion along the rings' array, $\delta q = -id/dx$, where x is the coordinate along the array measured in units of L. Making rescaling of this dimensionless coordinate, $2\sin\alpha\bar{x} = x$, we find $2\sin\alpha\delta q = -i\frac{\partial}{\partial\bar{x}}$. Finally, $\bar{\mathcal{H}}_1$ becomes a Hamiltonian of massive Dirac particle,

$$\bar{\mathcal{H}}_1 = \begin{pmatrix} \bar{\phi} - i\frac{\partial}{\partial\bar{x}} & h \\ h & -\bar{\phi} + i\frac{\partial}{\partial\bar{x}} \end{pmatrix}, \tag{45}$$

where $\bar{\phi} = 2\pi\delta\phi\cos\beta$ and $h = 2\pi\delta\phi\sin\beta\cos\alpha$. The dispersion of such Hamiltonian for a plane wave $e^{i\bar{q}\bar{x}}$ is given by $E^2 = (\bar{q}+\bar{\phi})^2 + h^2$, where

$$\bar{q} = 2\sin\alpha\delta q = -i\frac{d}{d\bar{x}}. \tag{46}$$

Let us now discuss localized states near the defects. We assume that there are two half-infinite regions of the array with different value of the flux. In the first region, at $x < 0$, the flux is smaller than $1/2$, $\phi = 1/2 - \delta\phi$, whereas in the second one, at $x > 0$, we have $\phi = 1/2 + \delta\phi$. The problem is fully analogous to the one discussed in Ref. [29]. Then at the interface between two regions there appear two (because Hamiltonian has two blocks) degenerate localized states of the Volkov-Pankratov type,

$$\psi_1^{\rm loc} = \begin{pmatrix} i \\ 1 \\ 0 \\ 0 \end{pmatrix} e^{-(|h|+i|\bar{\phi}|)|\bar{x}|},$$

$$\psi_2^{\rm loc} = \begin{pmatrix} 0 \\ 0 \\ 1 \\ i \end{pmatrix} e^{-(|h|-i|\bar{\phi}|)|\bar{x}|}. \tag{47}$$

Note that we removed the prefactor $(-1)^n = \exp(\pm i\pi x)$ from both functions, which corresponds to the shift $\delta q = q \pm \pi/2$ mentioned above. We see that the localization lengths of these localized states are equal. For $\delta v = 0$, the energy corresponding to these degenerate states lies exactly in the middle of the Dirac gap just as in the problem discussed in Ref. [29].

The localized topologically protected states obtained above form a two-level system, or qubit. The energy levels of this system depend on the parameter δv, which controls up-down asymmetry of the system. Changing δv by gate electrodes one can manipulate energy levels E_1 and E_2, which cross each other, for $\delta v = 0$, see Eq. (44). At this point, i.e., for the setup with up-down symmetry, the levels are doubly degenerate within the lowest approximation with respect to $\delta\phi$, δq.

C. Tunable topologically protected qubit

Projecting $H_{\rm eff}^{(1)} + H_{\rm eff}^{(2)}$ onto two localized states, Eq. (47), we get the Hamiltonian of the qubit formed by $\psi_1^{\rm loc}$ and $\psi_2^{\rm loc}$,

$$\mathcal{H}_{\rm qubit} = \begin{pmatrix} -W & \Delta_{\rm qubit} \\ \Delta_{\rm qubit}^* & W \end{pmatrix}, \tag{48}$$

Here, W depends linearly on δv according to Eq. (44), $\Delta_{\rm qubit} = \Delta_x + i\Delta_y = 2\pi\delta\phi^2\cot\alpha\sin\beta(\cos\alpha\cos\beta + i\sin\beta)$. Corresponding energy levels are given by

$$E_{\rm qubit}^{\pm} = \pm\sqrt{W^2 + |\Delta_{\rm qubit}|^2}, \tag{49}$$

where

$$|\Delta_{\rm qubit}| = 2\pi^2\delta\phi^2\sin\beta\cos\alpha\sqrt{\cot^2\alpha + \sin^2\beta}, \tag{50}$$

see Fig. 10.

The qubit is equivalent to a spin-1/2 in the "magnetic field"

$$\mathbf{B}_{\rm qubit} = (\Delta_x, \Delta_y, W). \tag{51}$$

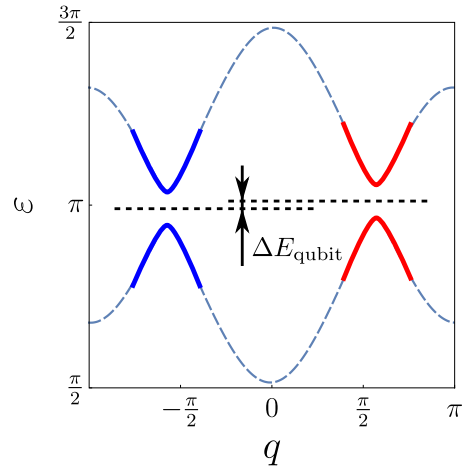

FIG. 10. Dispersion of the lowest band of the helical crystal for ($\alpha = \pi/5$, $\beta = 0.6$, $v = 0.07$, $\phi = 0.45$). The vertical distance between two DPs is controlled by v. Dashed lines shows positions of localized levels arising when the crystal has a defect. $\Delta E_{\rm qubit} = E_{\rm qubit}^{+} - E_{\rm qubit}^{-}$, see Eq. (49).

Most importantly, the "magnetic field" $\mathbf{B}_{\rm qubit}$ actually depends on the gate voltages and can be controlled in a pure electrical way. We notice also that such qubits exist in all bands, so that for high temperature there is an ensemble of $TL/v_{\rm F}$ qubits in the temperature window. These qubits can be coherently manipulated by gates and magnetic field.

V. EFFECT OF THE ELECTRON-ELECTRON INTERACTION

Next, we discuss effects of the electron-electron interaction on the properties of the crystal. It is known that the interaction strongly renormalizes the properties of the contact between two helical states [30,31], including spin asymmetry of the tunneling [32]. Here, we use renormalization group (RG) equations derived in Ref. [31] to find a general phase diagram of the helical crystal.

The problem of renormalization of the helical crystal is twofold. One aspect is the renormalization of the individual contact, which was discussed in [31]. Let us discuss now the second aspect, which is the peculiarity of the crystal geometry that restricts the renormalization by certain scale.

There are several relevant length scales in the problem: the Fermi wavelength λ_F (ultraviolet cutoff), $l_T = v_{\rm F}/T$ (thermal length), and ring size L. Corresponding energy scales are given by $E_{\rm F}$, T, and v_F/L (level spacing in a single ring). We assume that $E_{\rm F} \gg v_{\rm F}/L$ and $E_{\rm F} \gg T$. The relation between T and $v_{\rm F}/L$ can be arbitrary.

As discussed to some detail in Appendix D, we propose the following scenario. The renormalization of separate junctions happens at relatively high temperatures when the running energy scale is

$$E_{\rm F} > E > \max[T, v_{\rm F}/L], \tag{52}$$

(or, equivalently, the spatial interval lies between $\lambda_{\rm F}$ and $\min[L, l_T]$). When the temperature becomes low, $T < v_{\rm F}/L$, the junctions cannot be regarded as separate from each other

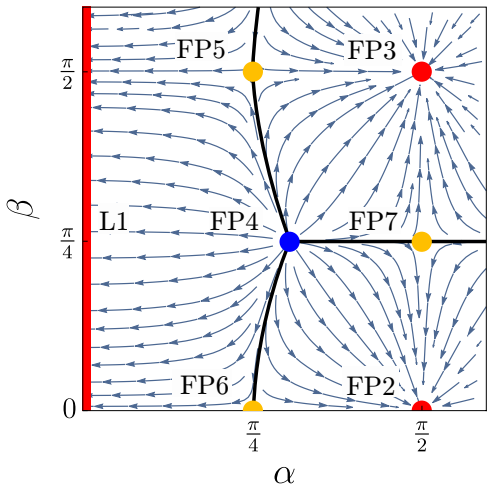

FIG. 11. Phase diagram and RG flows at the plane (α, β) [equivalent to Fig. 2(a) of Ref. [31] with corresponding change of parameters] Red color, the line of stable fixed points (L1) and two stable fixed points FP2 and FP3; blue color, fully unstable *multicritical* fixed point, FP4, separating three stable phases, corresponding to L1 (independent rings), FP2 (independent shoulders), and FP3 (spin-flip chiral channels); yellow color, three unstable saddle fixed point, FP5, FP6, and FP7. All fixed points are listed in the Table I.

and form an effective media. In other words, RG flow for the junctions' renormalization stops when T decreases below v_F/L.

Hence, interval (52) corresponds to independent renormalization of separate junctions, which is the case discussed in Ref. [31], see also [34]. Using Eq. (18) of Ref. [31] and assuming that the dimensionless interaction strength g in the helical state is small {so that the Luttinger parameter $K = [(1-g)/(1+g)]^{1/2}$ is close to unity, $K \simeq (1-g)$} we find RG flow in terms of α, β,

$$\frac{d\alpha}{d\Lambda} = -\frac{1}{8}g^2 \sin 2\alpha\left[2 - \sin^2\alpha\left(4 - \sin^2 2\beta\right)\right],$$
$$\frac{d\beta}{d\Lambda} = -\frac{1}{8}g^2 \sin^2\alpha \sin 4\beta. \tag{53}$$

Here $\Lambda = \log E_F/E$. We note that parameter v does not flow.

This set of equations defines the phase diagram of the RG flow in the plane (α, β) as shown in Fig. 11 (this diagram is equivalent to Fig. 2(a) of Ref. [31] with corresponding change of variables). The diagram contains a line of fixed points L1 and several fixed points FP2-FP7 shown by different colors: Red color, the line of stable fixed points L1, corresponding to $\alpha = 0$, and two stable fixed points FP2 $= (\pi/2, 0)$ and FP3 $= (\pi/2, \pi/2)$; blue color, fully unstable fixed point FP4 $= (\arctan\sqrt{2}, \pi/4)$; yellow color, three unstable saddle fixed points, FP5 $= (\pi/4, \pi/2)$, FP6 $= (\pi/4, 0)$, FP7 $= (\pi/2, \pi/4)$. All FPs are listed in the Table I.

TABLE I. Line of stable fixed points (L1) and fixed points (FP2-FP7) of interaction-induced RG flow in the plane (α, β). Stability is denoted by *s* (stable) or *u* (unstable).

No.	L1	FP2	FP3	FP4	FP5	FP6	FP7
α	0	$\pi/2$	$\pi/2$	$\arctan\sqrt{2}$	$\pi/4$	$\pi/4$	$\pi/2$
β	arbitrary	0	$\pi/2$	$\pi/4$	$\pi/2$	0	$\pi/4$
t	1	0	0	$1/\sqrt{3}$	$1/\sqrt{2}$	$1/\sqrt{2}$	0
r	0	1	0	$1/\sqrt{3}$	0	$1/\sqrt{2}$	$1/\sqrt{2}$
f	0	0	1	$1/\sqrt{3}$	$1/\sqrt{2}$	0	$1/\sqrt{2}$
Stability	s	s	s	u	u	u	u

We see that there are three stable phases in the crystal described by stable line L1, and stable points FP2 and FP3. Physics behind these phases is as follows: Stable line L1 corresponds to *independent rings*, when tunneling coupling between rings is zero and bands of the crystal shrink into discrete levels, Eq. (16). Stable point FP2 corresponds to *independent shoulders* of the rings array. Indeed, at this point we have $t = f = 0$, $r = 1$. As seen from Fig. 5, in this case upper and lower shoulders of the array are disconnected and electron moves without changing direction and chirality while passing contacts. Finally, FP3 corresponds to *spin-flip chiral channels*. At this point, $t = r = 0$, $f = 1$. This means (see Fig. 5) that electron makes spin-flip after each tunneling jump but does not change direction of the propagation.

Very interesting feature of the RG phase diagram is *multicritical* behavior. The fully unstable point FP4 separates three stable phases described above.

One can show that this phase diagram remains unchanged when taking into account higher order contributions in g [31].

VI. OUTLOOK AND CONCLUSIONS

Before concluding the paper let us outlook interesting problems for future research. As we demonstrated, two localized states, which appear on the boundary between regions having different radii of rings form a qubit placed in the effective "magnetic field" B_{qubit} [see Eq. (51)]. Actually, this field depends on gate voltages, so that the state of qubit can be manipulated purely electrically. Fabricating crystal with several boundaries between different regions allows one to create spatially separated qubits. By changing B_{qubit} (adiabatically or abruptly) one can study single qubit evolution and creation of entangled states involving qubits placed at different boundaries. Also, even at one boundary there can be many qubits for high temperatures, when temperature window covers many bands of the crystal and, consequently, involves many massive Dirac cones. Related tasks are electron-phonon dephasing and optical excitation of the ensemble of these spatially and/or energy separated qubits (analysis of quantum computing by an ensemble of energy separated qubits in a AB interferometer was presented in Ref. [19]).

There are also several directions of improvement of the developed model. In the above calculations of energies $E^{\pm}_{\text{qubit}}$ we assumed that both states forming qubit are inside the Dirac gap, $E^{+}_{\text{qubit}} - E^{-}_{\text{qubit}} < \Delta$. This inequality fails with increasing v. Study of the corresponding case of sufficiently large v implies analysis of the decay of qubit states into continuous spectrum. Another problem is related to the interaction-induced renormalization of the qubit parameters. Indeed, above we argued that RG flow stops with decreasing the temperature below level spacing in a single ring. This conclusion was based on the homogeneity of the interacting crystal. It fails in the presence of a defect. Hence, qubit parameters can

flow even at very low temperature. Note finally, that additional physics might appear for special models of edge confining potential, where edge reconstruction is possible [35].

Analysis of all these interesting problems is out of scope of the current paper and will be presented elsewhere. To conclude, we developed a theory of tunable helical crystal formed by periodic array of identical holes in a 2D topological insulator. We demonstrated that the tunneling transport through such array can be controlled by magnetic field and also by purely electrical way using various configuration of gate electrodes. For integer and half-integer values of the dimensionless flux through the holes, pairs of the Dirac points appear in each band of the spectrum. The positions of these points and the velocities at these points can be tuned by the gate voltages. Deviation of the flux from the special values leads to appearance of gap, i.e., corresponding Dirac cones become massive, and to convergence of the different Dirac points. The electron-electron interaction renormalizes properties of the crystal. We find the phase diagram and RG flows of the system in the plane of parameters (α, β) characterizing total and spin-flip tunneling couplings, respectively. We find that there are three different phases: independent rings, independent shoulders, and perfect spin-flip channels. There exist a fully unstable multicritical fixed point separating these phases.

We also derive an effective Hamiltonian of a defect in the crystal and show that topologically protected qubits can appear in the crystal within the gaps of the massive Dirac cones. These qubits can be controlled by purely electrical way. At relatively large temperatures, $T \gg v_F/L$, an ensemble of $N \sim TL/v_F$ topologically protected qubits appears. The possibility of purely electrical high-temperature control of these qubits opens a wide avenue for applications in the area of quantum computing.

ACKNOWLEDGMENTS

The work was funded by the Russian Science Foundation Grant No. 20-12-00147. The work of R.A.N. was partially supported by the Theoretical Physics and Mathematics Advancement Foundation "BASIS". Investigation of double Dirac points (Sec. III H) by R.A.N. was partially supported by a Grant of the President of the Russian Federation for state support of young Russian scientists - Candidates of Science, Project No. MK-2918.2022.1.2.

APPENDIX A: TRANSFER MATRIX

The transfer matrix $\hat{T}_0$, which connects amplitudes on the left and right sides of a contact is defined as follows:

$$\begin{pmatrix} C_3' \\ C_3 \\ C_4' \\ C_4 \end{pmatrix}_{(n+1)} = \hat{T}_0 \begin{pmatrix} C_2 \\ C_2' \\ C_1 \\ C_1' \end{pmatrix}_{(n)}. \tag{A1}$$

This definition allows one to find $\hat{T}_0$ by using matrix $\hat{S}_0$ [see Eq. (2)]. Direct calculation shows that $\hat{T}_0$ is given by Eq. (6).

While propagating inside a certain ring, the electron waves acquire phases that depend on electron energy as described by matrix Eq. (7), which connects amplitudes inside the ring as follows:

$$\begin{pmatrix} C_2 \\ C_2' \\ C_1 \\ C_1' \end{pmatrix}_{(n)} = \hat{P}_0 \begin{pmatrix} C_3' \\ C_3 \\ C_4' \\ C_4 \end{pmatrix}_{(n)}. \tag{A2}$$

By using gate electrode shown in Fig. 3 one can make different the energies for up and down part of the ring. Then matrix $\hat{P}_0$ becomes

$$\hat{P}_0 = \mathrm{diag}[e^{i\varphi_b^{\mathrm{up}}}, e^{-i\varphi_a^{\mathrm{up}}}, e^{i\varphi_a^{\mathrm{down}}}, e^{-i\varphi_b^{\mathrm{down}}}], \tag{A3}$$

where

$$\begin{aligned} \varphi_a^{\mathrm{up}} &= \varepsilon^{\mathrm{up}}/2 - \pi\phi, \\ \varphi_b^{\mathrm{up}} &= \varepsilon^{\mathrm{up}}/2 + \pi\phi, \\ \varphi_a^{\mathrm{down}} &= \varepsilon^{\mathrm{down}}/2 - \pi\phi, \\ \varphi_b^{\mathrm{down}} &= \varepsilon^{\mathrm{down}}/2 + \pi\phi, \end{aligned} \tag{A4}$$

and $\varepsilon^{\mathrm{up,down}} = k^{\mathrm{up,down}}L$. The meaning of these phases is the following. "Up" and "down" stand for the upper and lower shoulders of the ring. We assume that the upper and lower energies can be different in general by application of the different gate voltages to upper and lower shoulders of the ring, so that the kinematic phase $\varepsilon^{\mathrm{up,down}} = k^{\mathrm{up,down}}L$ can be different, too. Equations (8) are reproduced from Eq. (A4) when $\varepsilon^{\mathrm{up}} = \varepsilon^{\mathrm{down}} = \varepsilon$.

APPENDIX B: PHASES IN S MATRIX AND TRANSFER MATRIX

Observing symmetry with respect to time inversion, we should impose the following condition: $S^T = -ESE$ with $E = \mathrm{diag}[1, -1, 1, -1]$. This condition allows one to write the S matrix in the most general form given by Eq. (2). Corresponding transfer matrix is given by

$$\hat{T}_0 = \frac{e^{-i(\gamma_1+\gamma_2)}}{1-t^2} \times \begin{pmatrix} r_2 e^{i(\gamma_1+\gamma_2)} & f_1 t_2 & -f_1 e^{i(\gamma_1+\gamma_2)} & -r_2 t_2 \\ -t_1 f_2 & -r_1 & r_1 t_1 & f_2 \\ -f_2 e^{i(\gamma_1+\gamma_2)} & -r_1 t_2 & r_1 e^{i(\gamma_1+\gamma_2)} & f_2 t_2 \\ t_1 r_2 & f_1 & -f_1 t_1 & -r_2 \end{pmatrix}. \tag{B1}$$

Let us now assume the parametrization

$$\begin{aligned} \tau_1 &= (\gamma_1+\gamma_2)/2 + \delta\tau, \\ \tau_2 &= (\gamma_1+\gamma_2)/2 - \delta\tau, \\ \varphi_1 &= (\gamma_1+\gamma_2)/2 + \delta\varphi, \\ \varphi_2 &= (\gamma_1+\gamma_2)/2 - \delta\varphi. \end{aligned}$$

We notice that all phases in $\hat{T}_0$ can be removed by the following operation:

$$\begin{aligned} T_0 &= \hat{D}_1 \hat{T}_r \hat{D}_2, \\ \hat{D}_1 &= \mathrm{diag}[e^{i\gamma_2/2}, e^{i(\delta\tau-\delta\varphi-\gamma_2/2)}, e^{i(\gamma_1/2-\delta\varphi)}, e^{i(\delta\tau-\gamma_1/2)}], \\ \hat{D}_2 &= \mathrm{diag}[e^{i\gamma_2/2}, e^{i(-\delta\tau+\delta\varphi-\gamma_2/2)}, e^{i(\gamma_1/2+\delta\varphi)}, e^{i(-\delta\tau-\gamma_1/2)}], \end{aligned}$$

where $\hat{T}_r$ is given by above $\hat{T}_0$ with $\gamma_1, \gamma_2, \delta\tau, \delta\varphi$ put to zero. One can show that phases $\delta\tau, \delta\varphi$ do not enter dispersion equation for the spectrum of the crystal. Putting $\delta\tau = \delta\varphi = 0$, we arrive at Eq. (6) of the main text.

APPENDIX C: DOUBLE DIRAC POINTS

The positions of convergence points (q_j, ε_j) read

$$\begin{aligned}
&(q_1, \varepsilon_1) = (q_2, \varepsilon_2) = (\pi/2, 2\pi + 4\pi n) \text{ and} \\
&(q_1, \varepsilon_1) = (q_2, \varepsilon_2) = (-\pi/2, 4\pi n); \\
&(q_3, \varepsilon_3) = (0, -\pi + 4\pi n) \text{and} (\pm\pi, \pi + 4\pi n); \\
&(q_4, \varepsilon_4) = (0, \pi + 4\pi n) \text{and} (\pm\pi, -\pi + 4\pi n).
\end{aligned} \tag{C1}$$

Here n is integer. Coefficients D and E also depend on j, $D = D_j$, $E = E_j$, where

$$\begin{aligned}
D_2 = -D_1 &= \frac{2\sin\alpha\cos(v/2)}{\sqrt{1-\sin^2(v/2)\sin^2\alpha}}, \\
E_1 = -E_2 &= \frac{\cos^2\alpha\sin\alpha\sin(v/2)}{(1-\sin^2(v/2)\sin^2\alpha)^{3/2}}, \\
D_4 = -D_3 &= \frac{2\sin\alpha\sin(v/2)}{\sqrt{1-\cos^2(v/2)\sin^2\alpha}}, \\
E_4 = -E_3 &= \frac{\cos^2\alpha\sin\alpha\cos(v/2)}{(1-\cos^2(v/2)\sin^2\alpha)^{3/2}}.
\end{aligned} \tag{C2}$$

Above equations simplify for v close to 0 and π. For example, let us assume that

$$v = \delta v \ll 1, \tag{C3}$$

and consider point corresponding to $j = 4$. We get

$$\begin{aligned}
&\phi_4 \approx \frac{1}{2} + \frac{\alpha}{\pi} - \frac{\tan\alpha}{8\pi}\delta v^2, \\
&D_4 \approx -2\delta v\tan\alpha, E_4 \approx \tan\alpha.
\end{aligned} \tag{C4}$$

Expression for spectrum becomes

$$\begin{aligned}
&\delta\varepsilon \approx \delta q\delta v\tan\alpha \\
&\pm\sqrt{4\beta^2\sin^2\alpha + [\delta q^2\tan\alpha + 2\pi\delta\phi]^2}.
\end{aligned} \tag{C5}$$

Here, we assumed that

$$\beta \sim \delta\varepsilon \sim \delta\phi \sim \delta v^2 \sim \delta q^2 \ll 1. \tag{C6}$$

The spectrum simplifies even more and becomes symmetric with respect to δq for $\delta v = 0$,

$$\delta\varepsilon = \pm\sqrt{4\beta^2\sin^2\alpha + (\delta q^2\tan\alpha + 2\pi\delta\phi)^2}. \tag{C7}$$

As seen from Eq, (C7), for $\delta\phi < 0$, the spectrum has two close DP separated by distance $\delta q \propto \sqrt{-\delta\phi}$. Exactly at $\delta\phi = 0$, the DP converge. In this case, spectrum has a small gap $\Delta = 4\beta\sin\alpha$ at $\delta q = 0$, increases in a quatric way at small δq, and becomes parabolic at large δq with an effective "mass" depending on tunneling coupling only,

$$\delta\varepsilon = \pm\sqrt{4\beta^2\sin^2\alpha + \delta q^4\tan^2\alpha}. \tag{C8}$$

For positive $\delta\phi$, the gap increases,

$$\Delta \to 4\sqrt{\beta^2\sin^2\alpha + \pi^2\delta\phi^2},$$

and spectrum, Eq. (C7), becomes parabolic both at very small δq and very large δq, but with different effective masses. These cases are illustrated in Figs. 8(a)–(c). We also demonstrate in this figure [see Fig. 8(d)] asymmetric double DP spectrum corresponding to $\delta v \neq 0$ and $\delta\phi < 0$.

One more simple example of double DP is realized for v close to π at the point corresponding to $j = 2$. Then, $\phi_2 \approx 1 - \alpha/\pi + \delta v^2\tan\alpha/8\pi$, $D_2 = -\delta v\tan\alpha$, $E_2 = -\tan\alpha$. The spectrum is described by Eq. (C5) with the replacement $\delta v \to -\delta v$ and $\delta\phi \to -\delta\phi$.

APPENDIX D: RENORMALIZATION OF HELICAL CRYSTAL

In this Appendix, we justify the choice of the infrared cutoff in Eq. (52). Usually, e.g., in a single tunnel junction, renormalization arises due to virtual transitions involving energies E (counted from the Fermi energy) within the energy interval [36,37]

$$E_F > E > T, \tag{D1}$$

corresponding to the spatial scales between λ_F and l_T.

In a helical crystal the situation is more subtle and the choice of the infrared cutoff deserves a special discussion. The integration over all possible states within the interval (D1) can be represented as a summation over crystal band indices (stemming from single ring levels) and integration over wave vector q. Two limits $v_F/L \gg T$ and $v_F/L \ll T$ correspond to different physical situations (for discussion of similar problem of resonance defect formed by the two barriers in the Luttinger liquid separated by distance L see Ref. [38]).

In a simpler case of relatively high temperatures, $T \gg v_F/L$, the thermal length is shorter than L. Since the correlations between electrons are lost beyond the thermal length, the different junctions are renormalized separately, with l_T being the infrared cutoff. In this case, the temperature is high compared to characteristic band width, and $\sim v_F/L$, the specific structure of the bands is irrelevant.

At lower temperatures, when $l_T \gg L$, the interval (D1) can be split into two regions: $v_F/L < E < E_F$ and $T < E < v_F/L$. In the first region, we probe the scales shorter than L, so that one can consider renormalization of individual junctions. By contrast, in the second region, corresponding spatial scales are larger than L and RG flow should be discussed in terms of the crystal bands. More specifically, the Fermi level "picks" a certain band number N and a point in the dispersion curve corresponding to a certain q, and renormalization is determined by energies lying in this and neighboring bands. Individual rings and junctions play a role of building blocks of the effective uniform media. The consideration of phenomena happening at such scales cannot be described in terms of separate junctions. Instead, one starts with a consideration of interacting crystal with a certain dispersion curve $E_N(q)$. The next step is to linearize the spectrum near the Fermi level E_F corresponding to q_F, which obeys $E_F = E_N(q_F)$. The linearized spectrum is a starting point for

the description in terms of the Luttinger liquid. The parameters of such *homogeneous* liquid depend on the interaction strength in a trivial manner, they are either of marginal scaling dimension (in case as Fermi velocity) or irrelevant (dispersion curvature) [36,37]. The nontrivial renormalization occurs in this lowest-energy region only if we have a defect or distinct junction in this liquid. Particularly it implies that the properties of the above topologically protected qubit can be renormalized, which is an interesting problem on its own and should be discussed separately. Meanwhile we notice that the parameters of the energy band $E_N(q)$ are determined by those already renormalized parameters α, β, which are obtained by integrating out the running energies within the first region, $E > v_F/L$.

[1] B. Bernevig and T. Hughes, *Topological Insulators and Topological Superconductors* (Princeton University Press, Princeton, NJ, 2013).

[2] M. Z. Hasan and C. L. Kane, Rev. Mod. Phys. **82**, 3045 (2010).

[3] X.-L. Qi and S.-C. Zhang, Rev. Mod. Phys. **83**, 1057 (2011).

[4] C. L. Kane and E. J. Mele, Phys. Rev. Lett. **95**, 226801 (2005).

[5] B. A. Bernevig, T. L. Hughes, and S.-C. Zhang, Science **314**, 1757 (2006).

[6] M. König, S. Wiedmann, C. Brune, A. Roth, H. Buhmann, L. W. Molenkamp, X.-L. Qi, and S.-C. Zhang, Science **318**, 766 (2007).

[7] A. Roth, C. Brüne, H. Buhmann, L. W. Molenkamp, J. Maciejko, X.-L. Qi, and S.-C. Zhang, Science **325**, 294 (2009).

[8] G. M. Gusev, Z. D. Kvon, O. A. Shegai, N. N. Mikhailov, S. A. Dvoretsky, and J. C. Portal, Phys. Rev. B **84**, 121302(R) (2011).

[9] C. Brüne, A. Roth, H. Buhmann, E. M. Hankiewicz, L. W. Molenkamp, J. Maciejko, X.-L. Qi, and S.-C. Zhang, Nat. Phys. **8**, 485 (2012).

[10] A. Kononov, S. V. Egorov, Z. D. Kvon, N. N. Mikhailov, S. A. Dvoretsky, and E. V. Deviatov, JETP Lett. **101**, 814 (2015).

[11] H. Peng, K. Lai, D. Kong, S. Meister, Y. Chen, X.-L. Qi, S.-C. Zhang, Z.-X. Shen, and Y. Cui, Nat. Mater. **9**, 225 (2010).

[12] B.-C. Lin, S. Wang, L.-X. Wang, C.-Z. Li, J.-G. Li, D. Yu, and Z.-M. Liao, Phys. Rev. B **95**, 235436 (2017).

[13] J. H. Bardarson, P. W. Brouwer, and J. E. Moore, Phys. Rev. Lett. **105**, 156803 (2010).

[14] J. H. Bardarson and J. E. Moore, Rep. Prog. Phys. **76**, 056501 (2013).

[15] G. Gusev, Z. Kvon, O. Shegai, N. Mikhailov, and S. Dvoretsky, Solid State Commun. **205**, 4 (2015).

[16] P. Delplace, J. Li, and M. Büttiker, Phys. Rev. Lett. **109**, 246803 (2012).

[17] F. Dolcini, Phys. Rev. B **83**, 165304 (2011).

[18] R. A. Niyazov, D. N. Aristov, and V. Y. Kachorovskii, Phys. Rev. B **98**, 045418 (2018).

[19] R. A. Niyazov, D. N. Aristov, and V. Y. Kachorovskii, npj Comput. Mater. **6**, 174 (2020).

[20] R. A. Niyazov, D. N. Aristov, and V. Y. Kachorovskii, Phys. Rev. B **103**, 125428 (2021).

[21] R. A. Niyazov, D. N. Aristov, and V. Y. Kachorovskii, JETP Lett. **113**, 689 (2021).

[22] H. Maier, J. Ziegler, R. Fischer, D. Kozlov, Z. D. Kvon, N. Mikhailov, S. A. Dvoretsky, and D. Weiss, Nat. Commun. **8**, 2023 (2017).

[23] J. Ziegler, Quantum transport in HgTe topological insulator nanostructures, Ph.D. thesis, University of Regensburg, Regensburg, 2019.

[24] I. Knez, R.-R. Du, and G. Sullivan, Phys. Rev. Lett. **107**, 136603 (2011).

[25] S. Wu, V. Fatemi, Q. D. Gibson, K. Watanabe, T. Taniguchi, R. J. Cava, and P. Jarillo-Herrero, Science **359**, 76 (2018).

[26] F. Reis, G. Li, L. Dudy, M. Bauernfeind, S. Glass, W. Hanke, R. Thomale, J. Schäfer, and R. Claessen, Science **357**, 287 (2017).

[27] G. Li, W. Hanke, E. M. Hankiewicz, F. Reis, J. Schäfer, R. Claessen, C. Wu, and R. Thomale, Phys. Rev. B **98**, 165146 (2018).

[28] R. Stühler, F. Reis, T. Müller, T. Helbig, T. Schwemmer, R. Thomale, J. Schäfer, and R. Claessen, Nat. Phys. **16**, 47 (2020).

[29] B. A. Volkov and O. A. Pankratov, Sov. JETP Lett. **42**, 178 (1985).

[30] J. C. Y. Teo and C. L. Kane, Phys. Rev. B **79**, 235321 (2009).

[31] D. N. Aristov and R. A. Niyazov, Phys. Rev. B **94**, 035429 (2016).

[32] D. N. Aristov and R. A. Niyazov, Europhys. Lett. **117**, 27008 (2017).

[33] R. A. Niyazov, D. N. Aristov, and V. Y. Kachorovskii, JETP Lett. (to be publsihed).

[34] The renormalization was discussed in [31] in terms of dimensionless reduced conductances through a single junction, $G_R = (1-a)/2$ and $G_D = (1-b)/2$, which are connected to the angles α, β (β and γ in terms of [31], correspondingly) as follows: $a = 2\cos^2\beta\sin^2\alpha - 1$, $b = \cos 2\alpha$.

[35] J. Wang, Y. Meir, and Y. Gefen, Phys. Rev. Lett. **118**, 046801 (2017).

[36] H. J. Schulz, G. Cuniberti, and P. Pieri, *Fermi liquids and Luttinger liquids in Field Theories For Low-Dimensional Condensed Matter Systems* (Springer, New York, 2000), pp. 9–81.

[37] T. Giamarchi, *Quantum Physics in One Dimension*, The International Series of Monographs on Physics, Vol. 121 (Oxford University Press, Oxford, 2004).

[38] D. G. Polyakov and I. V. Gornyi, Phys. Rev. B **68**, 035421 (2003).